Large-scale Experiments on Breaching Flow Slides and the Associated Turbidity Current

Alhaddad, S.M.S.; Labeur, R.J.; Uijttewaal, W.S.J.

DOI
10.1029/2020JF005582

Publication date
2020

Document Version
Final published version

Published in
Journal of Geophysical Research: Earth Surface

Citation (APA)
Alhaddad, S. M. S., Labeur, R. J., & Uijttewaal, W. S. J. (2020). Large-scale Experiments on Breaching Flow Slides and the Associated Turbidity Current. *Journal of Geophysical Research: Earth Surface*, *125*(10), 1-21. Article e2020JF005582. https://doi.org/10.1029/2020JF005582

JGR Earth Surface

RESEARCH ARTICLE
10.1029/2020JF005582

Large-Scale Experiments on Breaching Flow Slides and the Associated Turbidity Current

Said Alhaddad[1], **Robert Jan Labeur**[1], **and Wim Uijttewaal**[1]

[1]Environmental Fluid Mechanics Section, Faculty of Civil Engineering and Geosciences, Delft University of Technology, Delft, The Netherlands

Key Points:
- We conducted novel experiments where nonvertical initial breach faces were tested, providing the first quantitative data for such conditions
- We provide direct measurements visualizing the structures of velocity and sediment concentration for breaching-generated turbidity currents
- Breaching-generated turbidity currents are self-accelerating; sediment entrainment and flow velocity enhance each other

Correspondence to:
S. Alhaddad,
S.M.S.Alhaddad@tudelft.nl

Citation:
Alhaddad, S., Labeur, R. J., & Uijttewaal, W. (2020). Large-scale experiments on breaching flow slides and the associated turbidity current. *Journal of Geophysical Research: Earth Surface*, *125*, e2020JF005582. https://doi.org/10.1029/2020JF005582

Received 20 FEB 2020
Accepted 3 SEP 2020
Accepted article online 14 SEP 2020

Abstract Breaching flow slides are accompanied by the generation of turbidity currents. Measurements of these currents are critical for understanding the interaction between the turbidity current and the slope surface, as well as for the validation of numerical models. However, there are insufficient data available detailing the velocity distribution or sediment concentration in these currents. This paper presents experimental results of unique large-scale physical model experiments on breaching flow slides conducted at the water lab of Delft University of Technology, The Netherlands. The model tests were carried out in a tank with a subaqueous sandy slope steeper than the internal friction angle for that sand. We performed a series of novel experiments in which various nonvertical initial slope angles were tested, providing the first quantitative data for such initial conditions. Measurements of flow thickness, velocities, and sediment concentrations are obtained, providing the spatial and temporal evolution of the turbidity currents and the resulting underwater slope morphology. The experimental results reveal that the breaching-generated turbidity currents are self-accelerating and that they dominate the problem of breaching flow slides. We evaluated the theoretical expression for the erosion velocity in the case of pure beaching—where the turbidity current has no influence on the erosion—and it overestimated the observed erosion. The analysis of the failure evolution showed that the sand erosion rate increases due to the acceleration of the turbidity currents downslope, until a certain threshold, leading to the steepening of the breach face and thus the occurrence of surficial slides.

1. Introduction

A flow slide occurs when a large, subaqueous soil mass is destabilized and accelerates down a slope, then eventually redeposits, creating a milder slope. This failure mechanism poses severe risk for subaqueous structures and is able to undermine an entire hydraulic structure, resulting in significant damage. Breaching is a specific type of flow slide, which is accompanied by the generation of turbidity currents. This type of current, from an engineering point of view, is very dangerous for the stability of structures placed at the seabed, such as oil pipelines, well heads, and cables. A breaching flow slide can thus pose dangers, directly and indirectly, to nearby or remote underwater infrastructure.

Many flow slide events, occurring in different places around the world, are reported in the literature (e.g., Koppejan et al., 1948; Kramer, 1988; Silvis & Groot, 1995). The Netherlands, in particular, has a long history of such events, where post-event observations were made. The absence of observations of the temporal development of the failure is due to the fact that flow slides usually remain entirely underwater and their timing is unpredictable. Sometimes, if the flow slide does not terminate underwater, it propagates to shorelines and riverbanks, where it may cause severe damages. A flow slide is inherently a complex failure mechanism, as it involves geotechnical aspects within the soil body and also hydraulic aspects within the fluid transporting the failing soil. Nevertheless, a thorough understanding of flow slides is important for enhancing the safety of flood defenses and designing well-suited mitigation measures.

The term "breaching" specifically refers to the gradual, retrogressive failure of a steep subaqueous slope, greater than the internal friction angle. This type of failure often occurs in densely packed sand, due to its dilative behavior under shear forces. Dilatancy results in a negative pore pressure, which temporarily stabilizes the sand. Due to the pressure difference, the ambient water is forced to flow into the pores, dissipating the negative pressure and, thus, destabilizing the grains located at the sand-water interface. These grains peel off one by one and get suspended in water. This failure mechanism has been used since the 1970s as a

means of sand mining by the Dutch dredging industry. To estimate the dredging production, Breusers (1977) introduced the term "wall velocity," which refers to the horizontal propagation speed of a vertical submerged slope due to the pure breaching process for which erosion is induced by gravity only. For the sake of consistency in this paper, we provide the resulting expression for the sand erosion velocity perpendicular to the breach face, v_w (m/s) (Alhaddad et al., 2020), which reads

$$v_w = -\frac{\sin(\phi - \alpha)}{\sin\phi}\frac{(1-n_0)}{\delta n}k_l\frac{\rho_s - \rho_w}{\rho_w}, \tag{1}$$

where ϕ is the internal friction angle, α is the slope angle, n_0 (-) is the in situ porosity of the sand, k_l (m/s) is the sand permeability at the loose state, ρ_s (kg/m^3) is the density of the particles, ρ_w (kg/m^3) is the density of water, and $\delta n = (n_l - n_0)/(1 - n_l)$ is the relative change in porosity, in which n_l (-) is the maximum porosity of the sand.

The suspension of sediments increases the fluid density, which in turn generates a turbulent flow referred to as a breaching-generated turbidity current. This current flows over and interacts with the slope surface. Consequently, it may increase the erosion of the sand surface, picking up more sediment into suspension, thereby increasing speed and erosion potential (Alhaddad et al., 2019). Quantitative data of the erosion caused by this current are still missing, leaving the question open whether it could play a considerable role in the problem of breaching flow slides. In this respect, it is worth mentioning that Equation 1 does not account for the sediment entrainment by turbidity currents; therefore, a few attempts were made to develop it into an erosion model accounting for sediment entrainment by turbidity currents (Mastbergen & Van Den Berg, 2003; Van Rhee, 2015). However, these erosion models show considerable differences in outcome for typical breaching conditions (Alhaddad et al., 2019), demonstrating the need for validation data.

It is quite difficult to carry out controlled in situ measurements of breaching and the associated turbidity currents, as the occurrence of these events is unpredictable in field situations and the turbidity currents may destroy the measuring instruments. This highlights the importance of laboratory studies for gaining better insights into the nature of breaching flow slides and their associated sediment transport. Very few laboratory experiments on breaching are reported in the literature (e.g., Eke et al., 2009; Van Rhee & Bezuijen, 1998; You et al., 2012). Moreover, these experiments have not sought to investigate the flow development along the breach face, instead focusing on investigating the failure evolution or turbidity currents traveling down the slope toe. Although breaching is theoretically a grain-by-grain failure, a periodic collapse of coherent sand wedges, referred to as surficial slide, was observed in some of these experiments. A complete theoretical description of these surficial slides is not yet available.

Very little is known about the structure of fluid velocity or sediment concentration of breaching-generated turbidity currents. The difficulties in measuring such currents, even in lab experiments, have resulted in there being very limited direct measurements of fluid velocity and concentration. There are several reasons why it is difficult to obtain such measurements. The development of breaching-generated turbidity currents is typically a nonuniform unsteady phenomenon, meaning that current kinematics and inner density distribution are space and time varying. Investigating the development of the current along the breach face demands a sufficient traveling distance and hence sufficient experimental scale. Besides, the generated turbidity currents are very thin (few centimeters), requiring high-resolution measurements to visualize their structure. Another complication is that the sediment bed (or "breach face") moves continuously backward as a result of sediment erosion. Crucially, the high sediment concentration within the current increases the difficulty level and limits the choices of possible measuring techniques.

This paper presents results of breaching experiments, properly scaled to warrant the occurrence of a self-accelerating turbidity current during the breaching process. The experiments are carried out in a 2 m high breaching tank in which the initial slope angle of the sand can be varied. Ultrasonic Doppler velocity profiling provided high-resolution, one-dimensional visualization of flow fields, thereby yielding the first quantitative visualization of velocity profiles of a breaching-generated turbidity current. In addition, wall-normal concentration profiles are provided. Furthermore, an analysis of the surficial slides is carried out, attempting to understand the reason behind their occurrence.

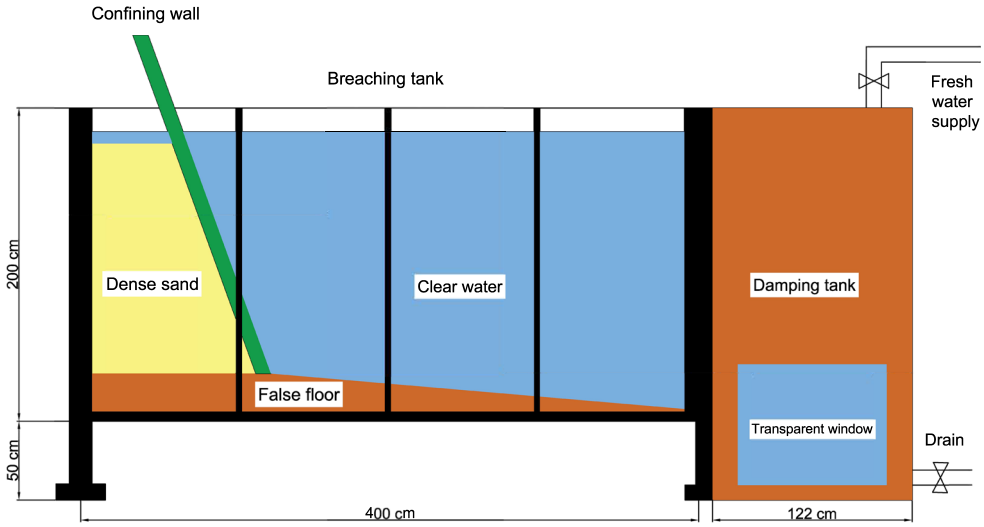

Figure 1. Side view of the experimental setup illustrating the components; the sedimentation tank is not shown in this figure.

2. Experiments

The experiments were set up specifically to investigate breaching flow slides and the associated turbidity currents. This section describes the design considerations and construction of the experimental tank, the instrumentation, the experimental procedures, and the processing of the results.

2.1. Experimental Setup

The experimental setup consists of several components: a breaching tank, removable confining wall, false floor, damping tank, and sedimentation tank. As triggering mechanisms of breaching flow slides are still poorly understood (Alhaddad et al., 2020), the experiments were performed for oversteepened, unstable slopes that initially fail due to the gravitational force. To this end, the slope of the confining wall can be adjusted in order to investigate a range of initial slope angles between 50° and 80°. The dimensions of the sand deposit were chosen such that the length of the breach face is similar in each of these experiments, ranging between 150 ± 10 cm. Figure 1 shows a schematic overview of the experimental setup; a description of each of its components is provided in the subsequent paragraphs.

2.1.1. Breaching Tank

The breaching process takes place inside this tank. Multiple factors were taken into account to determine the dimensions of this tank. One of these factors was to have a considerable contribution of the turbidity current to the erosion process along the soil-water interface. This contribution will be clearer once higher velocities of the turbidity current develop along the slope, causing high flow-induced shear stresses. For a given breach height, the layer-averaged downslope velocity of the turbidity current and the associated erosion rates can be estimated using the approximate layer-averaged three-equation model of Parker et al. (1986) (see Alhaddad et al., 2020). This was used to determine the required initial breach height and thus the breaching tank height.

The resulting breaching tank is 4 m long, 0.22 m wide, and 2 m high. It was made sufficiently long to allow for observation of the evolution of the breaching failure, both upstream as the breach face progressively erodes and downstream as the ensuing downstream turbidity current develops. The tank width was chosen to be similar to that of the flume at Utrecht University, The Netherlands, where geotechnical aspects of breaching flow slides are simultaneously being investigated. This would result in having comparable and complementary experiments. The back and front sides of our tank are made of different materials. The front side is made of glass to facilitate failure tracking and flow visualization. The back side is made of a removable steel plate making the tank accessible for maintenance purposes and to replace the false floor when required.

The false floor consists of two parts: a horizontal part on which the sand deposit is placed and a sloping part covering the distance from the toe of the sand deposit to the downstream end of the breaching tank. The false floor can be set to a specified slope, as to increase the sediment transport capacity of the turbidity

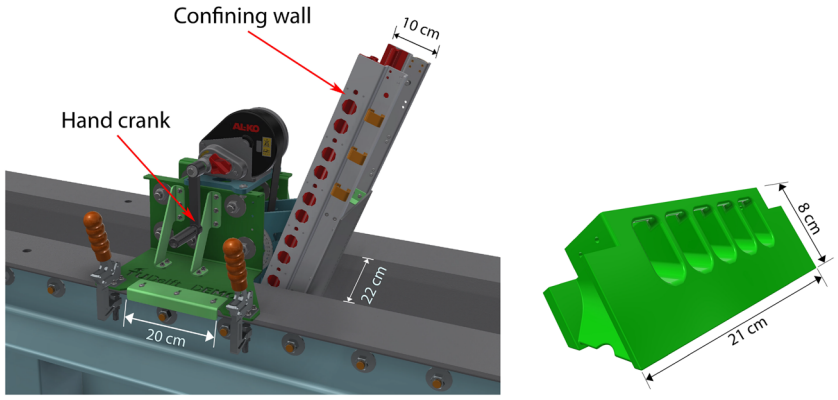

Figure 2. The confining wall: sketch of the support system placed at the top of the breaching tank (left) and the wall end (right).

current versus the existing flat bottom. Consequently, a less amount of sand will accumulate at the toe of the initial sand deposit, maintaining adequate breach heights during the experiments.

2.1.2. Confining Wall

A confining wall was needed to prevent the failure of sand during the construction process of the sand deposit and to shape the targeted slope angle. The used confining wall is a sliding mesh gate covered with geotextile (tissue opening size 0.04 mm), which allows water to pass through it while holding sediments in place. This enables water to escape from the pores through the wall to the ambient water during the compaction process of sand, creating a fully saturated densely packed deposit. A distinctive feature of this wall is that its inclination is adjustable, thereby allowing various initial slope angles.

The confining wall (230 cm long) is surrounded by a flexible rubber hose to prevent the soil particles from passing along the sides of the confining wall to the ambient water. The rubber hose was inflated with air before constructing the sand deposit to close all the gaps between the confining wall and the back and front sides of the breaching tank. The air was quickly released just before pulling out the confining wall to facilitate the pulling mechanism.

The confining wall is manually operated by a hand crank (Figure 2, left). A special support system was used to hold the confining wall in place during the construction of the sand deposit and during the pulling procedure. It also allows for horizontal adjustment of the wall along the breaching tank, making it possible to change the initial width of the sand deposit. A protractor fixed on the support system is used to adjust the inclination of the wall to the targeted slope angle. A different custom-built wall end was used for each experiment, as to avoid the escape of sediment particles at the slope toe (Figure 2, right).

2.1.3. Damping and Sedimentation Tanks

The downstream end of the breaching tank is left open and connected to a deeper damping tank (122 cm long, 114 cm wide, and 250 cm high) to allow the turbidity current to flow freely from the breaching tank into the damping tank. The level of the soil-water mixture in the damping tank should be kept below the bottom of the breaching tank to avoid reflection of the turbidity current from the damping tank back upstream. For this purpose, the turbidity current is drained from the bottom of the damping tank at the downstream end, while a flow of clear water is supplied at the top of the damping tank to maintain a constant ambient water depth throughout the experiment. The discharge of the inflowing water and outflowing turbidity current are monitored by electromagnetic flow meters. Additionally, two overflow pipes are used to make sure there is no water overspill.

The sedimentation tank (250 cm × 125 cm × 125 cm, adjacent to the damping tank, not shown in Figure 1) is used for collecting the sand-water mixture pumped out from the damping tank. It also allows the sand particles to settle down so the sand can be reused for the next experiments.

2.2. Characterization of Sand Deposit

As the problem of breaching is associated with fine sediments, a fine sand of d_{50} equal to 0.135 mm was used in the experiments. The analysis of the grain size distribution conducted within the Dutch-Flemish Western Scheldt monitoring program (Mastbergen & Schrijvershof, 2016) suggests that breaching mainly

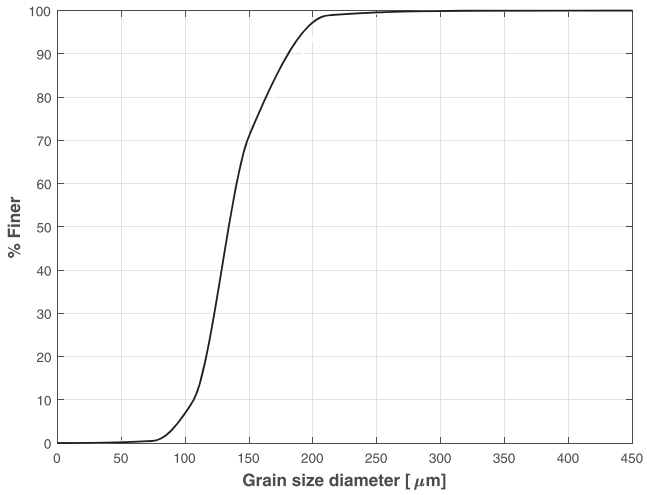

Figure 3. Cumulative grain size distribution of the sand used in the experiments.

occurs in uniformly graded sediment, motivating our choice of a uniformly graded sand. Figure 3 shows the cumulative grain size distribution of the sand used. The coefficients of uniformity, $C_u = d_{60}/d_{10}$ and curvature $C_c = d_{30}^2/(d_{60}\,d_{10})$, are 1.31 and 1, respectively, indicating that the sand is uniformly graded. In these relations, d_{10}, d_{30}, and d_{60} are particle sizes for which 10%, 30%, and 60% of the weight of the grains, respectively, is finer. As the range of the grain size distribution is small (Figure 3), the impact of segregation of finer and coarser grains, when pouring the sand into the breaching tank, is minimized.

The breaching process is largely determined by the permeability, the internal friction angle, and the initial and loose-bed porosity of the sand (see Equation 1). In order to define the permeability at maximum porosity, k_l, the permeability was measured for different porosities (Figure 4) through a series of constant-head permeability tests (ASTM-method D2434). The internal friction angle ϕ was as determined by the direct shear test. The initial porosity, $n_0 = 0.4$, and loose bed porosity, $n_l = 0.51$, were determined from sand compaction tests. The properties of the used sand are summarized in Table 1.

2.3. Test Procedure

Each breaching experiment was prepared following the next sequence of steps:

- The false floor is placed at the bottom of the breaching tank.
- The wall end corresponding to the selected slope is connected to the confining wall, in order to adjust the angle of the latter, after which the wall rubber is inflated with air.
- The tanks are half filled with clean water.
- A layer of sand (approximately 20 cm thick) is placed into the breaching tank and compacted by a vibrator needle until it cannot be further compacted (this ensures that the sand will be homogeneous and have the maximum relative density—minimum porosity).
- The previous step is repeated until the level of the top of sand deposit is few centimeters below the water level.
- Additional clean water is supplied into the tanks.
- The previous two steps are repeated until reaching the targeted breach height.
- The crest of the sand deposit is tapped by a wooden piece to make it horizontal.

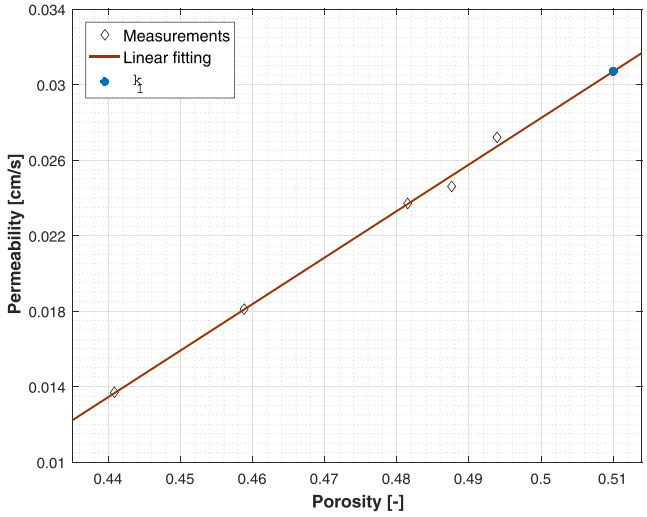

Figure 4. Sand permeability as a function of sand porosity; the permeability k_l is determined from the linear fitting.

After deploying the measurement instruments and testing their signals (see section 3), the experiment proceeds as follows:

- The wall rubber is deflated and the confining wall is quickly pulled out by rotating the hand crank, which takes about 6 s when operating the manual system at maximum rate; the experiment starts as soon as the confining wall is completely released.
- The turbidity current is drained from the bottom of the damping tank at the downstream end by a sand-water mixture pump while, simultaneously, a flow of clear water is returned at the top of the damping tank to guarantee a constant level of water in the tanks.
- The experiment stops if all the sediments from the sand deposit have run out, leaving a fresh deposit on the entire bottom of the tank.

Right after the removal of the confining wall, the underwater sand deposit starts to fail as particles peel off one by one, creating a shower of sand which drags the ambient water along to generate a downward turbidity current. Velocity and concentration profiles are measured at various transects normal to the breach face, for different stages of the breaching failure, following the development of the breach face and the associated turbidity current in time.

Table 1
The Properties of the Sand Used in the Experiments

d_{10}	d_{30}	d_{50}	d_{60}	n_0	n_l	ϕ	k_l
0.107 mm	0.123 mm	0.135 mm	0.140 mm	0.40	0.51	36°	0.0307 cm/s

Table 2 summarizes the initial conditions of the experiments conducted within this study.

3. Data Acquisition and Processing

3.1. Instrumentation

The underwater instruments are placed on a measuring post that can move over the breaching tank in the same direction as the breach face. The inclination of the lever (Figure 5) can be adjusted—using a rope connected to a friction cleat at the top part of the measuring post—in order to keep the instruments aligned with the breach slope as it evolves during the experiment. The measuring post was equipped with various instruments described in the following subsections.

3.1.1. Rakes of Siphons

Four rakes of three siphons each were used to obtain suspended sediment samples at different heights from the breach face in order to obtain the wall-normal density distributions. The sampling process was controlled manually for all siphons in all sets. All siphons were activated before the start of the experiments and were kept flowing constantly. The siphons were constructed from tubes of 8 mm external diameter and 5 mm internal diameter, large enough to allow for the flow of high-concentrated samples. The distance between the center of the first siphon and the breach face was not constant, and the central distance between siphons was fitted to 2 cm.

3.1.2. Ultrasonic Velocity Profilers

Simultaneous measurements of downslope flow velocity and acoustic backscatter were obtained using two units of Met-Flow ultrasonic velocity profilers (UVP-Duo). The UVP is a monostatic system, where the acoustic transducer works both as emitter and as receiver of the sound waves, to measure the radial velocity and backscatter along an axis perpendicular to the transducer face. The reader is referred to Lemmin and Rolland (1997) for further details on the capabilities and limitations of UVP.

Each UVP-Duo unit was equipped with two transducers, held in position by a custom-built holding house (Figure 6), where one transducer emits bursts of ultrasonic signals at a frequency of 1, 2, or 4 MHz. Initial experiments (70° and 80° initial slopes) revealed that high-resolution 4 MHz signals could not capture any velocities in the near-bed region, due to the high particle concentration, which attenuates the acoustic signal. It was, therefore, decided to use 1 and 2 MHz transducers in the rest of experiments, compromising spatial resolution. Two 2 MHz transducers were used at the upper part and two 1 MHz transducers at the lower part of the breach face. This gives a total of four transducers. The system is not able to obtain velocity profiles from every transducer simultaneously but can only obtain in sequence from each transducer. Consequently, two transducers in total were simultaneously recording. The ultrasonic signals involve 128 channels, directed along the transducer axis. The corresponding signals are reflected at the sand particles present in each channel. The transducer then records the frequency of the reflected signals. Using Doppler theory, the shift in emitted/received frequency determines the fluid velocity for every channel, which together produce a velocity profile.

Table 2
A Summary of the Initial Conditions of the Experiments

Test	Slope angle (°)	Breach face length (cm)	False floor angle (°)	Downstream distance[a] (cm)
1	80	144	6	284
2	70	156	6	284
3	65	140	9	245
4	60	156	9	245
5	50	160	13	214

[a]The downstream distance is the length of the slope down the toe of the breach face.

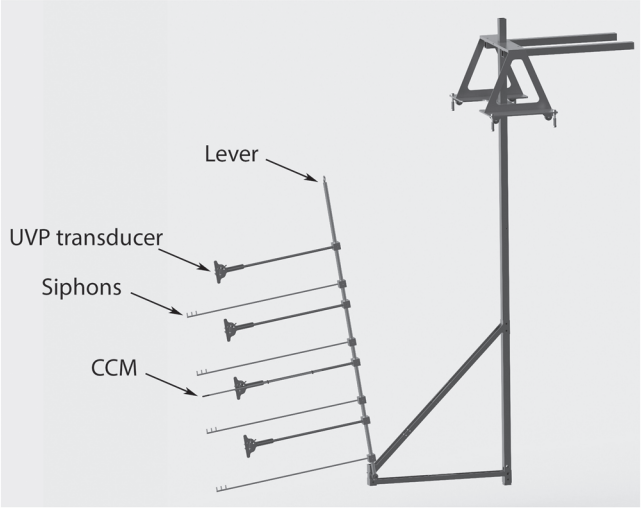

Figure 5. The measuring post with the instruments connected to the lever: four rakes of siphons, four ultrasonic velocity profiler (UVP) transducers, and one conductivity concentration meter (CCM).

3.1.3. Conductivity-Type Concentration Meter

The conductivity-type concentration meter (CCM) system is an instrument used to measure the concentration of sand-water suspensions at a single point. The measuring principle is based on the conductivity change of a sand-water mixture due to the change of the amount of suspended sediment present in the measuring volume. Conductivity-based instruments have been found most reliable for high sediment concentrations. The conductivity of the sand-water mixture is proportional to the density of the mixture. The CCM can measure sediment concentrations up to 50% by volume (Deltares, 2016). The volumetric sediment concentration C_v (-) can be measured using the following relation:

$$C_v = F_{\text{cal}} \left(1 - \frac{V_0}{V_m}\right) \tag{2}$$

where V_0 is the reference voltage for clear water, V_m is the measured voltage, and F_{cal} is the calibration factor. The voltages for clear water and for different sand-water mixtures, using the same type of sand as used in the experiments, were used to derive the value of F_{cal}.

3.1.4. Video Cameras

Besides the measuring post, two digital video cameras (25 frames per second) were employed to record the entire experimental run. The view of the first camera was set on the sand deposit to measure the erosion rate along the breach face and to define the position of siphons and the angle of the UVP transducers with the vertical. On the other hand, the view of the second camera was set on the entire breaching tank to investigate the overall failure evolution. A checkerboard pattern and horizontal and vertical rulers were placed on the

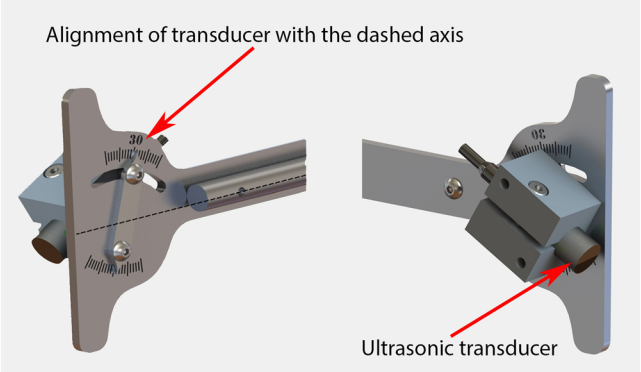

Figure 6. The holding house of the UVP transducers; in all experiments the transducer angle was set to 30° with the dashed axis, the latter roughly corresponding to the normal of the breach face.

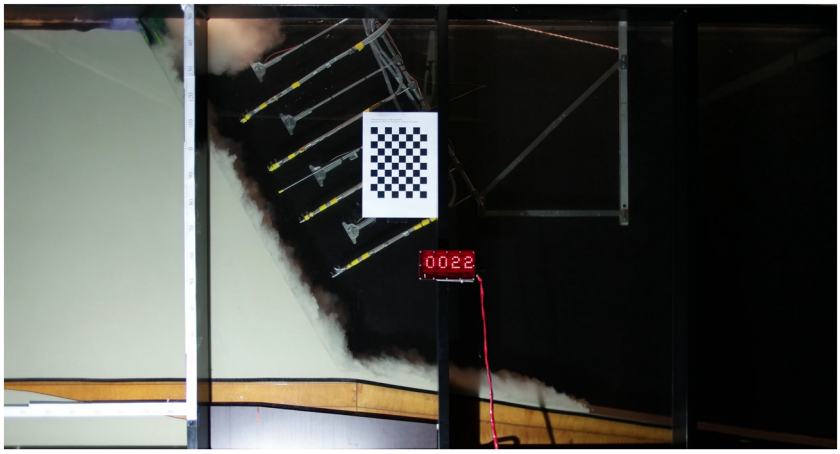

Figure 7. Generation of a plume of sand particles upon the removal of the confining wall during the 60° experiment. The digital clock refers to the time of the UVP measurements, and the checkerboard was used in combination with the horizontal and vertical rulers for camera calibration.

front side of the tank to be used as a reference frame for correcting the extrinsic distortion of the camera images; see Figure 7.

3.2. Data Acquisition

As soon as the confining wall is completely released, the measuring post is moved toward the breach face to collect data; see Figure 7. A plume of sand particles would be generated very near the slope surface by the quick release of the confining wall. The measurements start right after the settlement of the first plume particles, which usually takes a few seconds. Focus was set on the initial stage of the failure, when the slope angle was the same everywhere along the breach face.

Care is taken to ensure that the majority of the siphons are located within the current before obtaining the siphon samples. This is done by maneuvering the lever and the measuring post. The samples were taken at four points along the breach face. Each siphon sampled a volume of 0.1 L at three different elevations along the wall normal, sometimes at just one or two elevations due to the thinness of the current or misplacement of siphons. The misplacement could be a result of having the lever not sufficiently parallel to the breach face or having a breach face of a variable slope. The samples were taken seven times, at different instances, during each experiment as the slope failure evolves (Figure 8). These samples were later analyzed for sediment concentration by weighing and drying the samples.

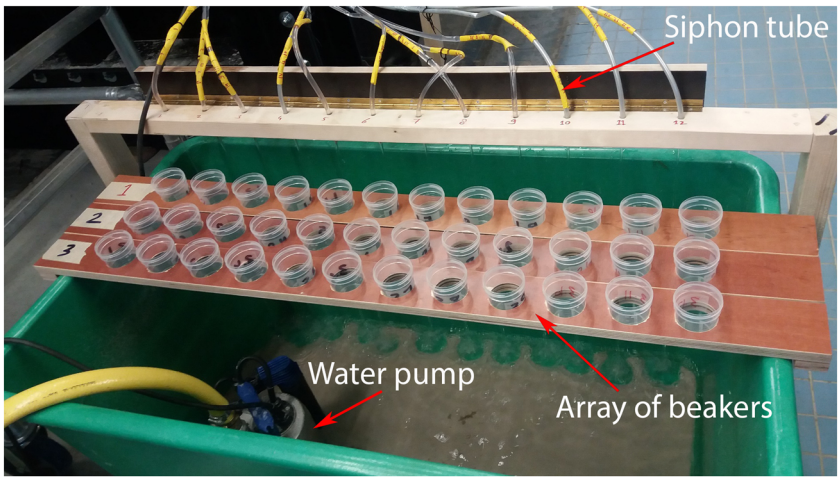

Figure 8. The technique of collecting the siphon samples: The array of beakers is pushed forward to simultaneously collect the samples coming through the tubes in the beakers; the water pump is used to avoid the overspill of water.

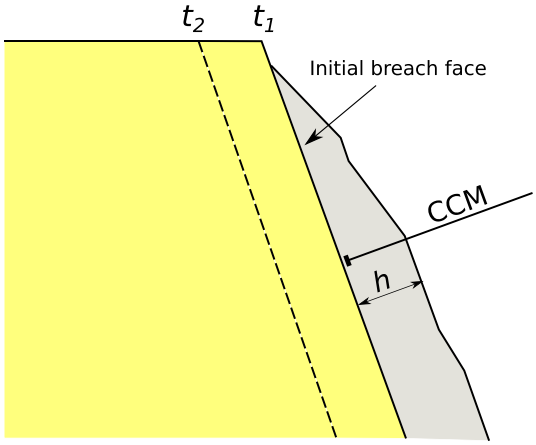

Figure 9. Measuring concept by the CCM: t_1 is the initial time and t_2 is the final time for the concentration measurements of a certain concentration profile; the dotted line refers to the breach face at t_2.

Regarding the UVP measurements, attention was paid to the distance between the transducers and the breach face. This is because the transducers have a certain measurement window within which they can measure velocities. The measuring post is kept in place as long as possible to provide sufficient time for the velocity measurements. It is horizontally moved from time to time due to the retrogressive erosion of the breach face. Care was taken to have the lever of the measuring post as parallel as possible to the slope. Toward this end, the inclination of the lever had to be adjusted from time to time due to the steepening of the breach face. The measurements taken during the adjustment of the measuring post are entirely ignored.

The tip of the CCM probe is initially placed as close as possible to the breach face to measure the majority of the concentration profile at the selected measuring point. The position of the CCM is kept constant in space while the breach face is progressively moving backward due to the erosion process (Figure 9). In this way, assuming a steady flow, the concentration profile can be obtained.

Monitoring the breach face changes during each experiment allowed the reconstruction of time-varying bed profiles. These proved useful in calculating the erosion rate at different positions along the breach face as well as the rate of deposition of sediment at and beyond the breach toe. Bed elevation changes were easily estimated from the video and still photographs. Turbidity current thicknesses were determined from still photos and from the velocity profiles obtained by the UVP transducers.

3.3. Data Processing

3.3.1. Velocity Profiles

The temporal resolution for each of the four UVP transducers was 74–90 ms (the actual measurement time is a function of the selected velocity resolution, which is a function of the frequency of the transducers). The raw velocity data were first filtered for unwanted spikes and noise; a three-point moving mean replaced all data outlying two standard deviations (see Figure 10). The time-averaged velocity profiles are a result of averaging 40 successive instantaneous profiles, covering about 3 s (Figure 11).

The UVP transducers were positioned almost in the middle of the tank width. Due to the transverse concavity of the breach face (see section 4.3.3), it was not possible to pinpoint the bed position at the transducers directly from the video recordings. Therefore, as to further analyze the data, the bed position was assumed to coincide with the position of the minimum velocity captured in the near-bed region, which was determined from the time-averaged velocity profile. It is to be noted that this assumption is not necessarily correct

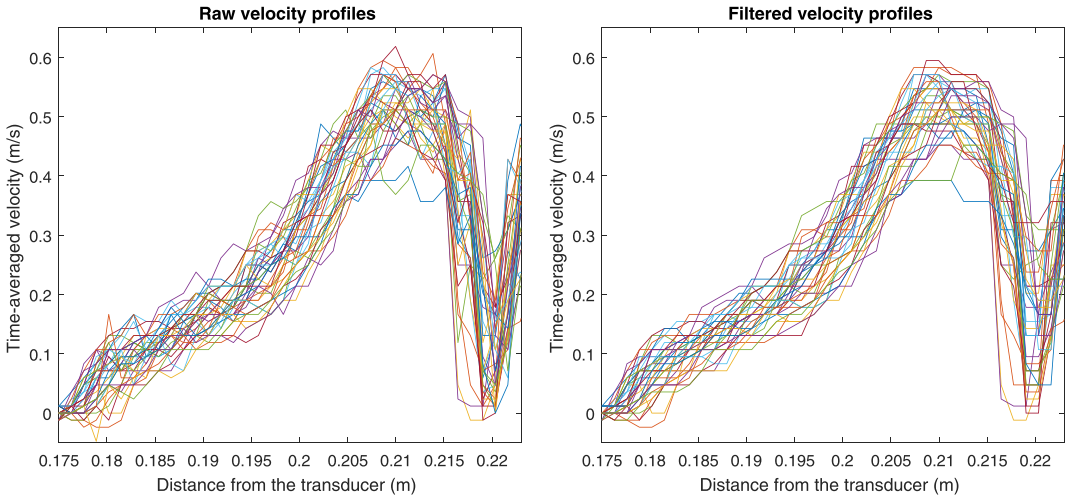

Figure 10. UVP data processing: raw velocity profiles 50° experiment (left) and filtered velocity profiles (right).

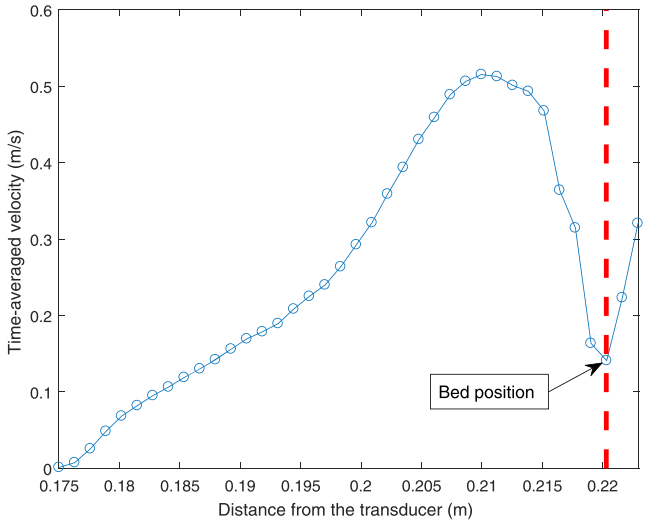

Figure 11. Time-averaged velocity profile for the 50° experiment showing reconstruction of the bed position; each marker represents a point where velocity data is available.

and might affect the self-similarity analysis of the velocity profiles (see section 4.2.1). Figure 11 shows some velocity recordings beyond the derived bed position, which is due to reflection of the signal off the bed and therefore ignored in the analysis. Also, in the near-bed region, the velocity of the current should presumably vary from 0 (at the bed) to a higher velocity (above the bed), which is clearly not the case in the velocity profiles obtained by the UVP (see Figure 13). This artifact is caused by the high near-bed particle concentration, leading to some noise in the instantaneous velocity profiles, and by the movement of the breach face (at a rate of a few millimeters per second) during the averaging interval for the mean velocity profiles.

3.3.2. Concentration Profiles

Concentration profiles are partially acquired from the measurements conducted on the flow samples obtained by the siphons. The samples, taken at different heights from the breach face, provide time-averaged values of the particle concentration on the time span—about 6 s—necessary to fill the sample. The UVP backscatter signal was thus calibrated with siphon samples and used for estimating suspended sediment concentration profiles. The reader is referred to Pedocchi and García (2012) for a detailed description of the inversion of the acoustic intensity measured with the UVP to acquire suspended sediment concentrations.

The particle concentrations of breaching-generated turbidity currents are high, particularly near the bed, attenuating the acoustic signal. As a consequence, the derived concentration profiles by the UVP backscatter signal do not cover the entire layer thickness. The missing part of the concentration profiles in the near-bed region is therefore estimated by fitting an interpolation function to the concentration profile. The concentration profiles obtained by the CCM (see Figure 15) confirmed that an exponential fit is sufficiently accurate for this purpose. At the bed position, which is obtained from the UVP measurements, a densimetric particle concentration is assumed of 1,298.5 kg/m^3, corresponding to the maximum (or loose-state) porosity of 0.51. In this way, an estimate of the entire concentration profile can be obtained that corresponds to the simultaneous velocity profile.

3.3.3. Layer-Averaged Quantities

Using the velocity and concentration profiles, it is possible to determine the associated characterizing height h (m), layer-averaged velocity U (m/s) and layer-averaged volumetric concentration C (-) of the turbidity current based on the following relations (Garcia & Parker, 1993; Parker et al., 1986, 1987):

$$Uh = \int_0^{z_\infty} u\,\mathrm{d}z, \tag{3}$$

$$U^2 h = \int_0^{z_\infty} u^2\,\mathrm{d}z, \tag{4}$$

$$UhC = \int_0^{z_\infty} cu\,\mathrm{d}z, \tag{5}$$

where u (m/s) is locally averaged streamwise flow velocity, c (-) is the local concentration of suspended sediment, z (m) is upward-normal coordinate, and z_∞ is the height at which the local velocity u is 0. The quantities h, U, and C are obtained by solving the system of Equations 3–5.

Figure 12. The experiment in progress: the turbidity current and the deposition of sediments in the downstream region.

4. Experimental Results

4.1. General Failure Description

Upon removal of the confining wall, the underwater sand deposit started to fail as particles peel off one by one, creating a shower of sand which drags the ambient water along to generate a downward turbidity current

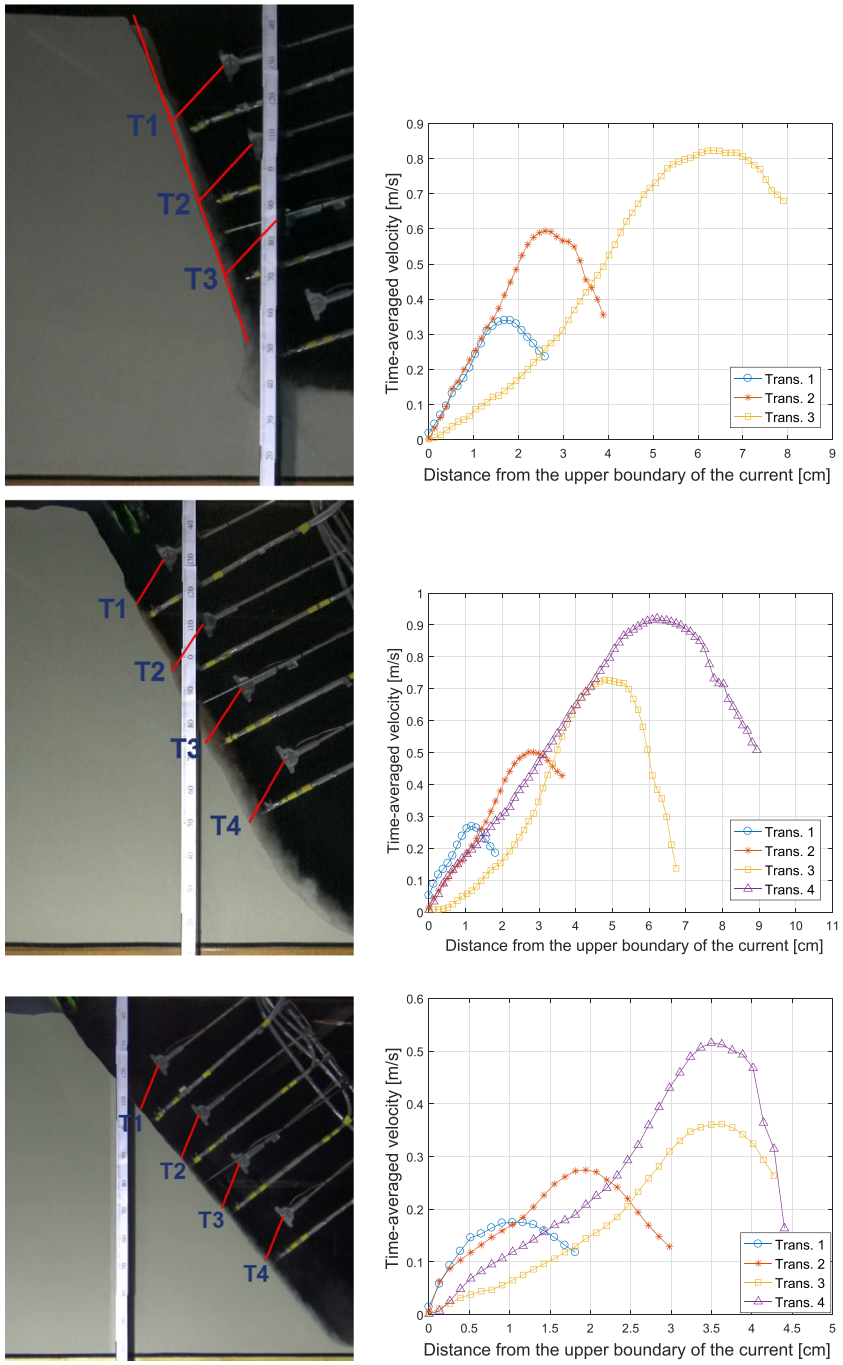

Figure 13. Positions of the UVP transducers (left panels) and corresponding profiles of the mean flow velocity (right panels): 70° slope—initially 65° (top), 64° slope—initially 60° (middle), and 50° slope—initially 50° (bottom).

(see Figure 12). This current makes a turn at the slope toe and propagates as a net-depositional current over the downstream region, where it exchanges sediments with the bed through erosion and deposition processes. In contrast to the current along the downstream region, no distinct current head was formed for the current along the breach face (Figure 7), as the sand particles fail everywhere along the breach face. The sediment started depositing at the breach toe, where the current made a turn. The current downstream of the breach toe emplaced a wedge-shaped deposit with a much milder slope than the breach face. The final slope of the deposit accumulated at the downstream region (see Figure 12) ranges from 13° to 21° with lower values corresponding to steeper initial breach faces.

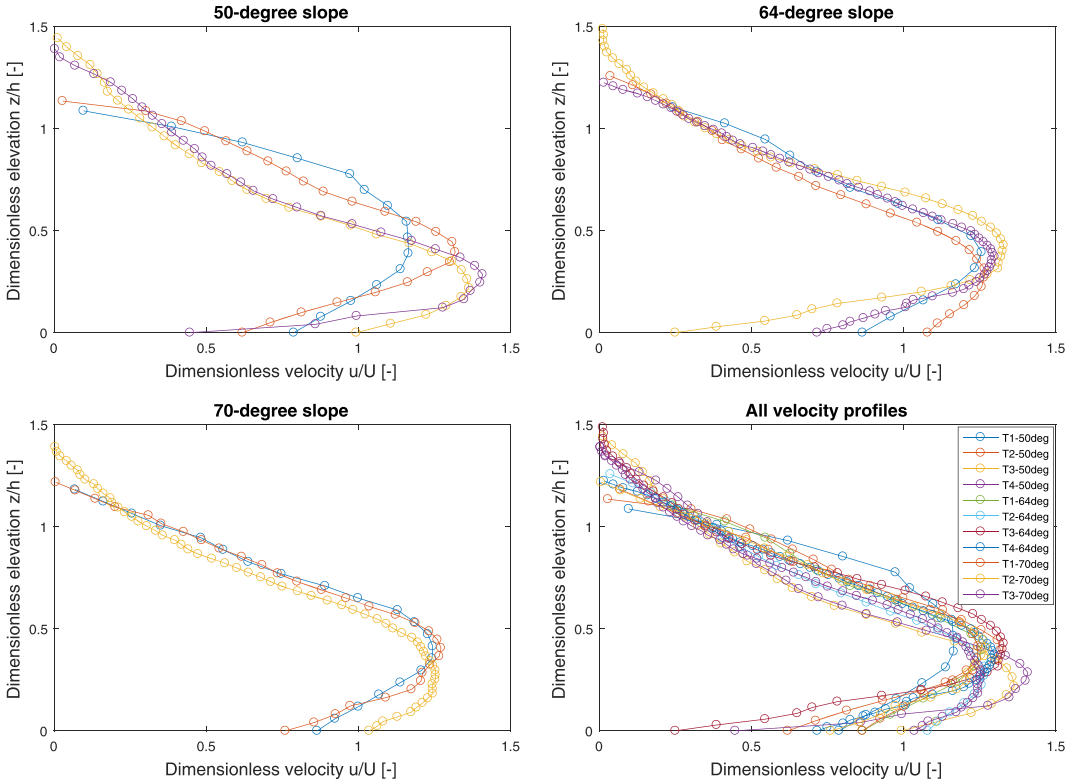

Figure 14. Dimensionless velocity profiles: 70° slope—initially 65° (top left), 64° slope—initially 60° (top right), 50° slope—initially 50° (bottom left), and all slopes (bottom right).

An overhang develops from time to time, leading to the slide of an internally coherent sand wedge (surficial slide) and then the uppermost part of the breach face would relax toward a milder slope (see Figure 23). The retreat of the breach face and the ensuing sand deposition at and beyond the breach toe resulted in a breach face that migrated upstream and gradually decreased in height. The retrogressive erosion lasts until a slope smaller than the internal friction angle is formed.

In the following, we will first analyze the turbidity current by considering velocity and concentration profiles and the overall development of the suspension layer along the breach slope, respectively. To focus the analysis on the spatial variability of the flow, results will be documented for situations when the slope angle was almost constant along the breach face, which reduces the number of variables. Spatially varying breach slopes will be considered when analyzing the sand erosion along the slope resulting from the turbidity current. Finally, we will consider the influence of the turbidity current relative to the gravity.

4.2. Analysis of the Turbidity Current

4.2.1. Velocity Profiles

Figure 13 shows measured profiles of the mean streamwise flow velocity together with the corresponding in situ positions of the UVP transducers, for momentary slope angles of 70°, 64°, and 50°, with initial slopes of 65°, 60°, and 50°, respectively. For the 70° slope, the velocity profile of Transducer 4 is not reported in Figure 13, top right, due to the local interference of the turbidity current with the bed downstream of the breach face; see also Figure 13, top left.

The observations clearly demonstrate the characteristic velocity profiles associated with breaching-generated turbidity currents. Moving up from the breach face, the velocity rapidly increases, reaching the maximum located in the near-bed region of the current. Beyond the peak, the velocity gradually decreases to become 0 at the interface of the current with the ambient water. Generally, the peak velocity increases with the streamwise distance along the slope and with the steepness of the slope, reaching maximum values up to 0.90 m/s in our experiments. The thickness of the velocity layer (or velocity profile) develops in a similar fashion, increasing from typically one to a few centimeters near the crest of the slope to 5–9 cm near

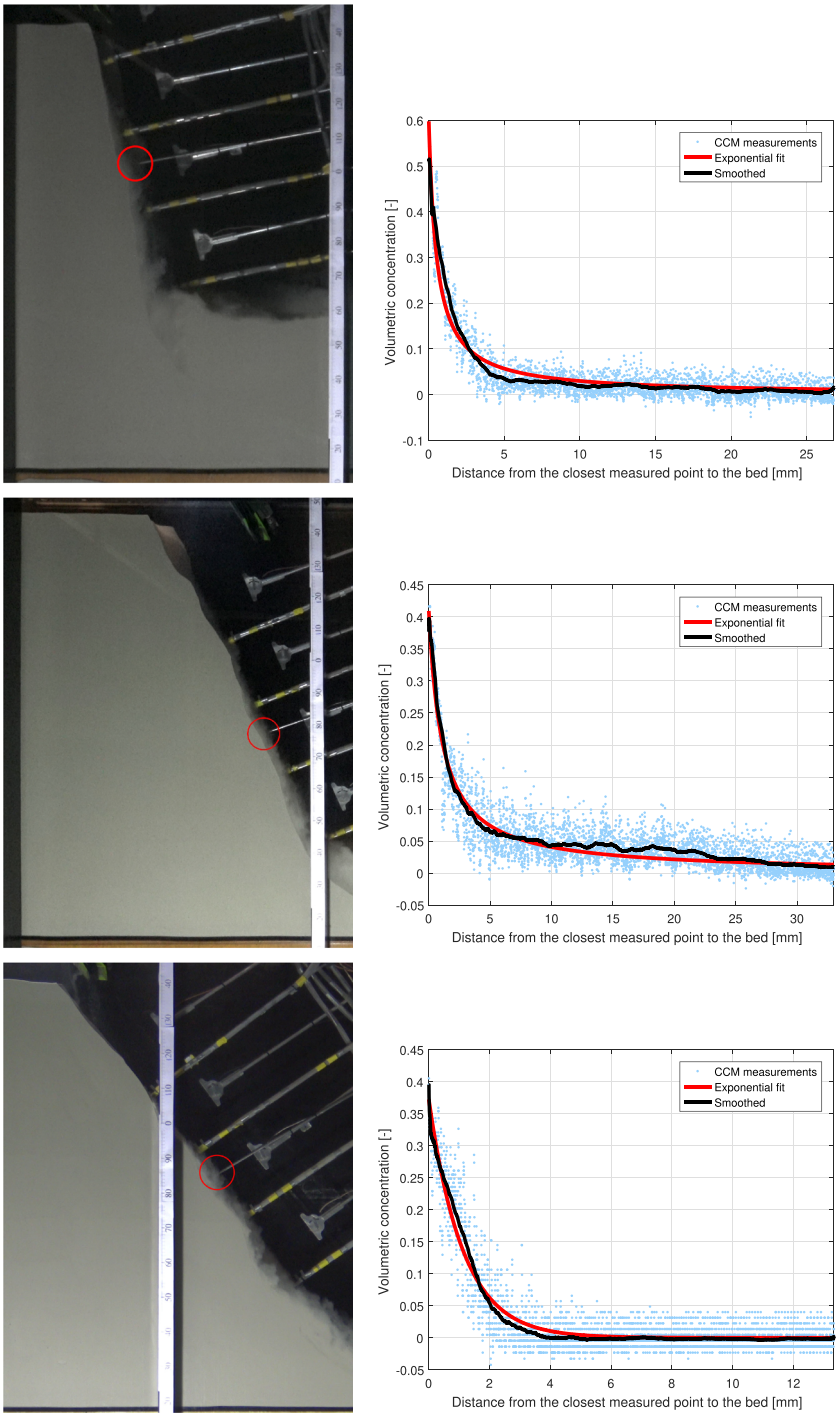

Figure 15. Location of the CCM probe (left panels) and corresponding sediment concentration profiles (right panels): 77° slope (initially 65°) at 42 cm from the crest (top), 67° slope (initially 65°) at 74 cm from the crest (middle), and 54° slope (initially 50 degrees) at 71 cm from the crest (bottom); the black lines indicate concentration profiles averaged over a 1 s sampling interval, while red lines indicate an exponential fit.

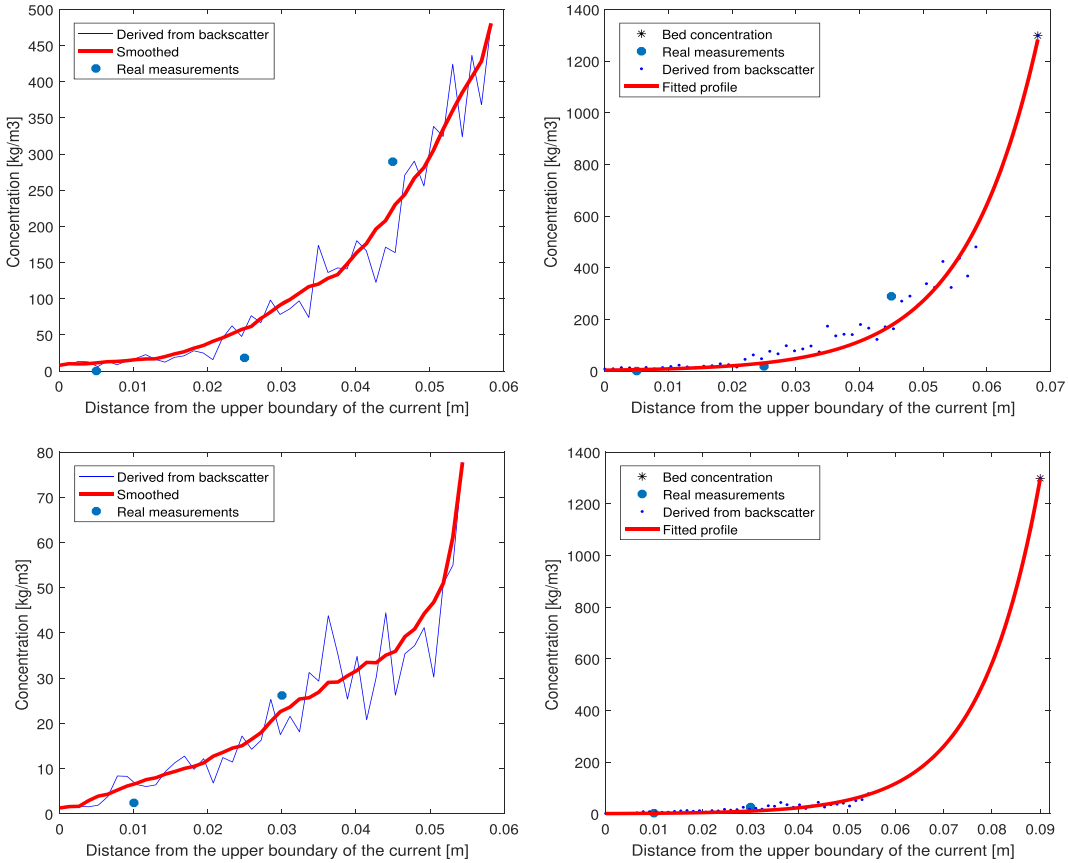

Figure 16. Concentration profiles for a slope of 64° (initially 60°): Transducer T3 at 81 cm from the crest (top), Transducer T4 at 106 cm from the crest (bottom); left panels show incomplete concentration profiles derived from acoustic backscatter measurements (blue line), concentrations from the siphon samples (blue dots), and smoothed (red line) concentration profiles; right panels show concentrations from the siphon samples (large blue dots), calibrated concentrations (small blue dots), inferred bed position and concentration (asterisks), and fitted exponential concentration profile (red line).

the toe, with the largest thicknesses occurring for the steeper slopes. The development of the layer-averaged flow velocity along the slope is analyzed in section 4.2.3.

To assess whether or not the observed velocity profiles are self-similar, nondimensional velocity profiles are shown in Figure 14, in which the flow velocity and distance to the bed have been scaled with, respectively, the layer-averaged velocity U and the layer thickness h as obtained from Equations 3–5. Indeed, the results suggest self-similarity, moreover so for Transects 3 and 4 further down the slope. For Transect 1, especially that of the 50° slope, self-similarity cannot be demonstrated convincingly because the uncertainty in the derived bed position is relatively large compared to the associated layer thickness.

4.2.2. Concentration Profiles

Concentration profiles derived from the CCM measurements and the corresponding in situ probe locations are shown in Figure 15, for momentary slope angles of 77°, 67°, and 54°, with initial slopes of 70°, 65°, and 50°, respectively. The measurements are smoothed over 1 s time intervals, using a moving average filter, to obtain time-averaged concentration profiles. The momentary distance from the tip of the fixed probe to the moving bed, needed to calibrate each profile, was determined from the observed erosion rate at the respective CCM position.

At the start of the measurements, the tip of the CCM was positioned almost at the bed capturing volumetric concentrations of about 0.5, for every experiment, which nearly matches the assumed maximum concentration of 0.49 at the bed. Away from the breach face, normal to the bed, the concentration swiftly decreases over a small distance and then slightly decreases to reach 0 at the upper boundary of the current (right panels of Figure 15). The region near the bed, where the concentration decreases rapidly, has a thickness of

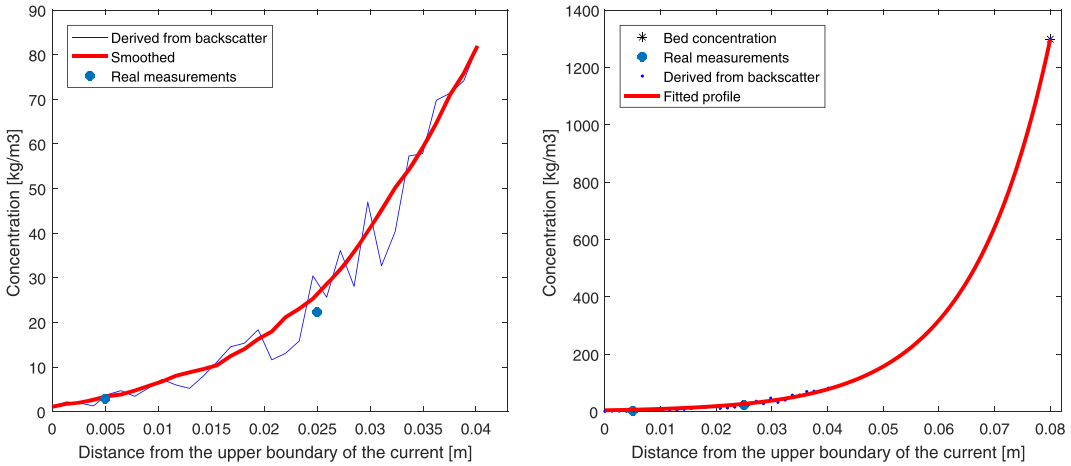

Figure 17. Concentration profiles for a slope of 70° (initially 65°) at Transducer T3, 76 cm from the crest: Left panels show incomplete concentration profiles derived from acoustic backscatter measurements (blue line), concentrations from the siphon samples (blue dots), and smoothed (red line) concentration profiles; right panels show concentrations from the siphon samples (large blue dots), calibrated concentrations (small blue dots), inferred bed position and concentration (asterisks), and fitted exponential concentration profile (red line).

about 5 mm for the 77° and 67° slopes, while for the 50° slope the thickness of only 2 mm is comparatively small. It should be noted that a direct comparison of the profiles is not possible as they relate to different positions along the slope. However, the measurements confirm that the concentration decays exponentially away from the bed.

The acoustic backscatter measurements provide simultaneous data of concentrations and velocities for the same transect, which requires calibration with the siphon samples. A sufficient number of adequate samples could be obtained for relatively thick layers only, specifically, for Transects T3 and T4 of the 64° slope (initially 60°) and for Transect T4 of the 70° slope (initially 65°). At all other transects, the layer was too thin to collect more than one siphon sample. All the obtained concentration profiles do not cover the near-bed region and are therefore interpolated from the observed data points using an exponential fit, as confirmed by the CCM measurements. At the bed position, which is inferred from the velocity data, a volumetric sediment concentration of 0.49 is imposed. The resulting concentration profiles are shown in Figures 16 and 17 and will be used further on to assess the spatial development of the layer-averaged concentration.

4.2.3. Layer-Averaged Properties

Layer-averaged quantities are obtained from the UVP velocity transects and the corresponding calibrated and interpolated concentrations, using Equations 3–5.

Figure 18 shows a comparison of the spatial development of the turbidity currents based on the slope angle. The results show that the layer-averaged velocity of the turbidity current increases in the downstream direction (Figure 18) as a result of the increased suspended sediment concentration (see Table 3) due to sand entrainment from the breach face (see Figure 19). In other words, the turbidity current strengthens itself in the downstream direction. This implies that the breaching-generated turbidity currents are self-accelerating (Sequeiros et al., 2018). Unsurprisingly, the steeper the slope, the higher the flow velocities and the larger the flow thicknesses. Turbidity currents over a steeper bed tend to have higher downward velocities and simultaneously a larger volume of entrained water from the upper boundary, which increases the layer thickness in the downstream direction.

Table 3 summarizes the main flow and sediment transport characteristics at four locations separated by a distance of 24 cm for the 64° slope (initially 60°). It can be noticed that the flow at these locations is supercritical (Froude number $Fr_d > 1$), which is likely a necessary condition for the occurrence of self-accelerating turbidity currents (Sequeiros et al., 2018). Furthermore, the sediment transport increases significantly in downslope direction, which is attributed to the increased total discharge in the current rather than the layer-averaged concentration—which hardly varies between these locations. This observation confirms the important role played by the water entrainment at the upper boundary of the layer. As such, this will largely

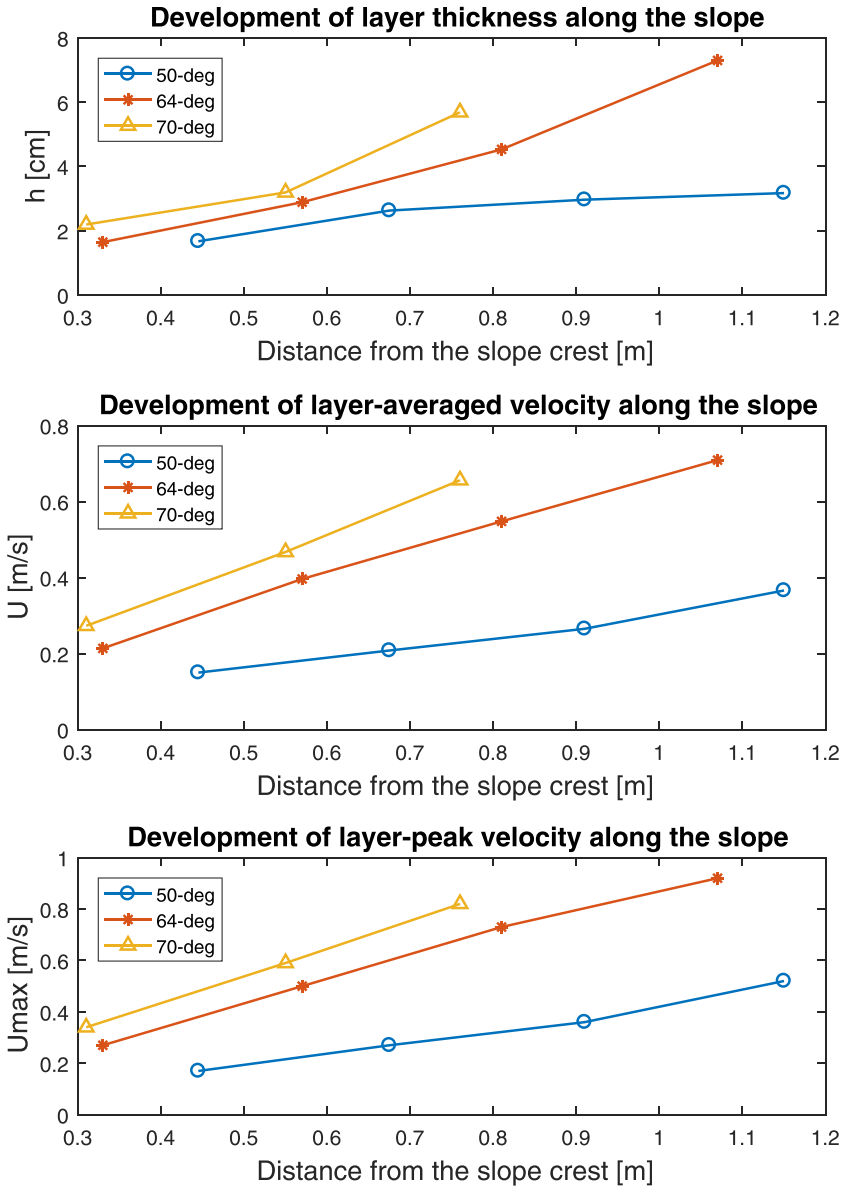

Figure 18. Comparison of spatial evolution of turbidity currents propagating over 50°, 64°, and 70° slopes: layer thickness development (top), layer-averaged velocity (middle), and layer-peak velocity U_{max} (bottom).

Table 3
Main Characteristics of the Flow and Sediment Transport at Four Locations Along the 64° Slope (Initially 60°)

Transducer	X (m)	U (m/s)	h (m)	Uh (m^2/s)	C (-)	UhC (m^2/s)	S_s (kg/m^2)	Fr$_d$ (-)	Ri (-)	e_w (-)	v_{ent} (mm/s)	Re $\times 10^3$ (-)
T1	0.33	0.21	0.016	0.003	n.a.	n.a.	n.a.	n.a.	n.a.	n.a.	n.a.	3.17
T2	0.57	0.40	0.029	0.012	0.08	0.0010	5.3	2.04	0.241	0.0059	2.35	10.94
T3	0.81	0.55	0.045	0.025	0.10	0.0025	14.7	2.04	0.241	0.0059	3.22	23.35
T4	1.06	0.71	0.073	0.052	0.08	0.0041	15.8	2.31	0.188	0.0074	5.22	48.90

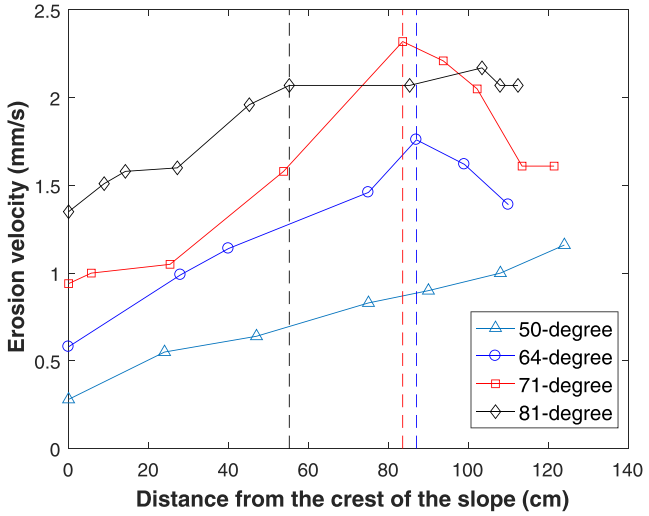

Figure 19. Erosion rate perpendicular to the breach face along slopes of different angles, calculated over a time interval of 15 s; the vertical, dashed lines refer to the transitions in erosion behavior.

determine the gradient of the downslope sediment flux leading to steepening and collapsing of the slope morphology.

The water entrainment coefficient e_w, which is a function of the bulk Richardson number $Ri = 1/Fr_d^2$, can be calculated using the relation proposed by Parker et al. (1987). The values of Fr_d and thus the corresponding values of Ri and e_w are consistent with the range of values reported in the literature (e.g., Sequeiros, 2012). The rate of water entrainment $v_{ent} = Ue_w$ is also presented in Table 3. The results show that e_w and v_{ent} tend to increase in the streamwise direction, meaning that larger volumes of water entrain into the turbidity current, thereby increasing the flow thickness while slowing down the flow.

To show the self-accelerating behavior of the current even more clearly, we present the amount of suspended sediment S_s (kg/m^2) within the current at each cross section, which is defined here as the area under the concentration profile. The results show an increase of S_s in the downstream direction similar to the increase of U and U_{max}, evidencing that the increase of the flow velocity is caused by the increase of the particle concentrations.

4.3. Analysis of Slope Failure

4.3.1. Erosion Rate

The erosion rate is defined here as the sand erosion velocity perpendicular to the breach face. Understanding how the erosion rate varies along the breach face is not only required to accurately predict the total erosion rate by breaching, it is also crucial to understand the evolution of the slope failure. The erosion rates at different points along the breach face, as measured from the video recordings, are shown in Figure 19. Generally, the erosion rate of the breach face increases in the downstream direction of the slope. This increase is due to the acceleration of the associated turbidity current in the downstream direction as a result of the increasing concentration of suspended sediments. In this way, the sediment entrainment and acceleration of the turbidity current are coupled in a positive feedback loop.

However, for slope angles steeper than 50°, there is a transition where the erosion rate starts to decrease, or becomes constant, further down the slope (Figure 19). The steeper the slope, the closer to the crest this transition occurs. The reason for this transition was not investigated in this work, but we speculate that it is related to turbulence damping. The turbidity current, driven by the suspended sediments, involves a turbulence shear stress, which causes the resuspension of sediment. However, the resulting density stratification will also dampen the turbulence. The self-enhancing process can therefore only continue until turbulence production and damping are in equilibrium (Cantero et al., 2012). Based on this argument, it is expected that the erosion rate for 50° slope would also transition, if only further downstream than what was possible to document in the performed experiment. Sequeiros et al. (2009) have reported self-accelerating turbidity currents to become depositional with increasing sediments size, suggesting such a transition.

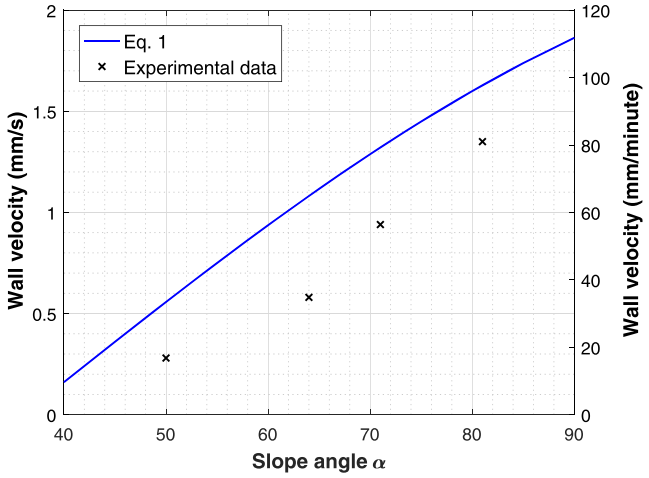

Figure 20. Comparison between computed wall velocity (using Equation 1) and measured wall velocity (15 s mean).

All this does not yet mean that the gravity-induced, grain-by-grain failure (absence of flow-induced erosion) is only of minor importance. Rather, this mechanism of "pure breaching" initiates the slope failure and determines the erosion at the crest of the slope, thus providing the initial and boundary conditions for any mathematical model of slope erosion. We therefore compare the physics-based equation for the wall velocity (Equation 1) with the observed erosion rates. To this end, the erosion rates at the crest and some neighboring points—where the velocities of the turbidity current are almost 0—are derived from the video measurements and averaged. The obtained value is considered the erosion rate for pure

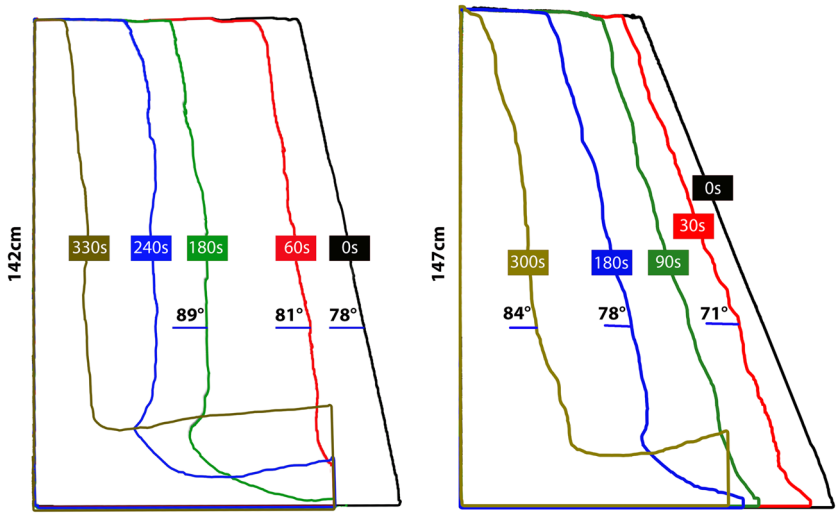

Figure 21. Slope steepening during breaching: 80° experiment (left) and 70° experiment (right).

breaching. The comparison with Equation 1 is shown in Figure 20 for four slope angles corresponding to the range of the experiments. This comparison shows that the overall agreement between the theoretical expression and the experimental results is quite good, although the theoretically derived wall velocity tends to overestimate the erosion rate of pure breaching. In particular, the trend with respect to the slope angle, α, is reproduced well indicating that Equation 1 captures the relevant physics consistently.

4.3.2. Breach Face Morphology

The temporal bed morphology evolution (Figure 21) distinctly demonstrates that the lower part of the breach face erodes more quickly than the upper part, resulting in the steepening of the breach face over time. The process underlying this steepening is the self-enhancing turbidity current causing an increasing sediment erosion in downslope direction. This steepening also leads to the occurrence of so-called surficial slides, intermittent failures due to confined slope overhangs, which will be discussed in the next subsection. Note while inspecting the failure evolution that surficial slides might have taken place between two consecutive bed profiles. The slope evolution is, therefore, not entirely governed by the entrainment of sediment from the breach face.

It has also been clearly observed that the breach face is not uniform across the breach face. The erosion is highest almost in the middle between the tanks walls and declining toward the walls. In other words, the breach face assumes an inward curve, looking into the direction of the erosion (Figure 22). This is consistent with the final morphology of breaching events reported in the literature, which also take a concave shape (e.g., Beinssen & Mastbergen, 2017). The combination of video recordings and UVP measurements shows that the location of the breach face at the tank walls may differ from its location in the middle of sand width by a distance of 2 to 3 cm. This shape remains fairly stable during the progression of the breach face. This equilibrium shape implies a laterally uniform backward erosion velocity, while the erosion velocity normal to the breach face decreases toward the tank wall. It is conjectured that the latter is not only a result of deviating soil properties near the wall (e.g., permeability and shear strength) but is also related to the lateral structure of the turbidity current. This implies that the three-dimensionality of the current and of the soil structure, respectively, plays an important role in the breaching problem.

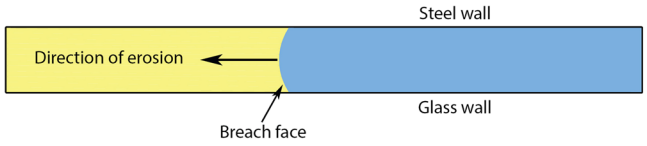

Figure 22. Sketch of the top view of the sand deposit showing the nonuniformity of the erosion across the breach face.

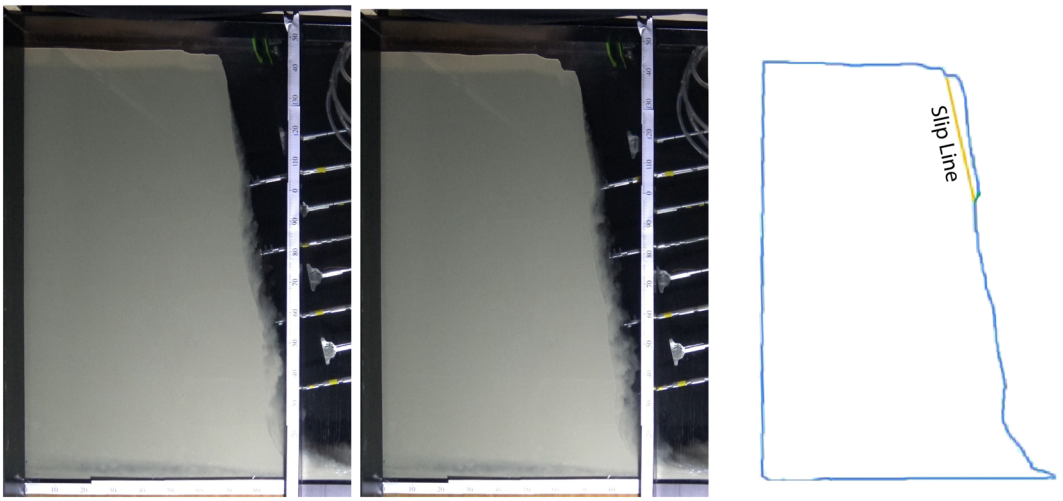

Figure 23. An example of surficial slides, experiment of 80° initial slope: just before the surficial slide (left), ongoing surficial slide (middle), and slip line (right).

4.3.3. Surficial Slides

As the lower part of the breach face erodes faster than the upper part, the breach face steepens over time. This steepening leads to overhanging and ultimately the collapse of a coherent mass of sediment, referred to as a "surficial slide" (Figure 23). These slides are always found to take place at the uppermost part of the breach face.

The surficial slides were tracked through the video recordings to find out more about their physics. The frequency, average area, and average sliding velocity of the surficial slides were determined for three different experiments (Table 4). It was found that all of these characteristics correlate with the angle of the breach face; steeper slopes lead to more frequent slides, larger slides and higher sliding velocities. Also, the shear stress acting on the slip plane due to the overhang weight, just before the occurrence of the slides, was calculated from the slid areas and masses (not included in Table 4). Interestingly, for more than 75% of the surficial slides, the shear stress prior to sliding was between 130 and 140 N/m^2. This implies that the overhang slides downslope under the pull of gravity when the shear stress on the slip plane exceeds the shear strength of the sand.

Surficial slides temporarily enhance sediment erosion and the suspended sediment concentration, rendering the flow even denser and thus faster. Figure 24 shows a local, sudden increase in the concentration profile measured by the CCM due to a small surficial slide. It remains to be investigated how important the intermittent surficial slides are for the bulk behavior of the turbidity current and the associated overall evolution of the slope.

4.3.4. Relative Influence of Gravity and Turbidity Current

Even though breaching in the first place is a gravity-induced failure, the generated turbidity current seems to start dominating the failure just after its onset until the final deposition of the sediments. This argument is based on several reasons. The turbidity current accelerates rapidly and could become capable of entraining sediments from the breach face more than the sediments falling due to the gravitational force (see Figure 19). Besides, it was shown that the turbidity current could be the primary reason why the surficial slides take

Table 4
Statistical Analysis of Surficial Slides Observed Through the Glass for Three Different Experiments

Initial slope angle (°)	60	70	80
Number of slides (-)	8	10	20
Sliding frequency (Hz)	0.019	0.033	0.056
Average slid area (cm^2)	27.81	32.56	3.66
Average sliding velocity (cm/s)	2.92	3.66	5.28

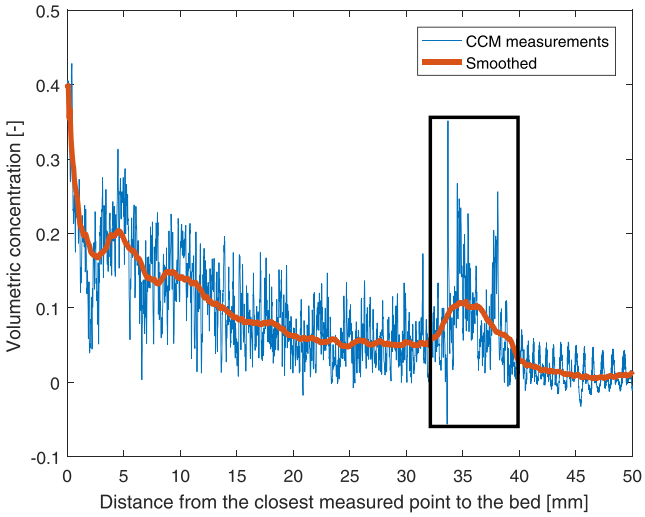

Figure 24. Abrupt increase of sediment concentration due to an observed small surficial slide, experiment of 65° initial slope.

place. Furthermore, the run-out distance and hence the fate of the sediments are governed by the hydrodynamics of the turbidity current. Crucially, the influence of the turbidity current determines whether the breaching process is stable (the height of the breach face decreases over time) or unstable (the height of the breach face increases over time). A complete physics-based theory for this influence is not yet available, but Van Rhee (2015) presents an empirical relationship to predict whether the breaching process is stable or unstable.

5. Conclusion

The results from a series of physical experiments on breaching flow slides reveal that breaching-generated turbidity currents are self-accelerating; sediment entrainment and flow velocity enhance each other. Consequently, the erosion rate of the breach face increases in the downstream direction of the slope until a certain threshold, possibly due to turbulence damping. Although breaching is essentially gravity-induced failure, the accompanied turbidity current dominates the failure evolution. This implies that successful numerical simulations of breaching flow slides must be capable of reproducing the hydrodynamics and sediment transport of turbidity currents. The expression of wall velocity generally coincides with measured erosion rate of pure breaching but tend to overestimate it. This fact should be accounted for when attempts are made to extend the expression of wall velocity to an erosion model including sediment entertainment by turbidity currents. Finally, the variation of the erosion rate along the breach face leads to the oversteepening of the lower part of slope. As a result, a sediment overhang develops and eventually slides downslope under the pull of gravity, when the shear stress on the slip plane exceeds the shear strength of the sand. These slides considerably enhance local sediment erosion, implying that they should be incorporated in breaching erosion models.

Acknowledgments
This study was conducted as a part of the MPM-Flow project "Understanding flow slides in flood defences." This project is funded by The Netherlands Organisation for Scientific Research (NWO) (Grant 13889). We would like to thank University of Twente for lending us Ultrasound Doppler Velocity Profilers (UVP), Utrecht University for lending us 1 MHz transducers, Dr. Matthew Czapiga for his assistance in designing the measuring post, and TU-Delft lab technicians for their assistance during the experimental work.

Data Availability Statement

A supplementary data set of selected experiments including videos is available at 4TU.ResearchData (https://doi.org/10.4121/uuid:bb06e47d-cd39-432d-8cce-1afd97e76049).

References

Alhaddad, S., Labeur, R. J., & Uijttewaal, W. (2019). The need for experimental studies on breaching flow slides. In *Proceedings of the second international conference on the material point method for modelling soil-water-structure interaction* (pp. 166–172). Cambridge, UK.

Alhaddad, S., Labeur, R. J., & Uijttewaal, W. (2020). Breaching flow slides and the associated turbidity current. *Journal of Marine Science and Engineering*, *8*(2), 67.

Beinssen, K., & Mastbergen, D. R. (2017). Flow slides: Understanding their geo-mechanical mechanisms, the threats they pose and how these threats can be managed. In *13th hydraulics in water engineering conference* (pp. 132). Engineers Australia

Breusers, H. N. C. (1977). Hydraulic excavation of sand. In *Proceedings International Course in Modern dreding*. The Hague, The Netherlands. 5–10 June 1977.

Cantero, M. I., Shringarpure, M., & Balachandar, S. (2012). Towards a universal criteria for turbulence suppression in dilute turbidity currents with non-cohesive sediments. *Geophysical Research Letters*, *39*, L14603. https://doi.org/10.1029/2012GL052514

Deltares (2016). Conductivity type concentration meter. https://www.deltares.nl/app/uploads/2016/04/CCM-Conductivity-type-concentration-meter.pdf, Online; accessed 15-08-2018.

Eke, E., Parker, G., & Wang, R. (2009). Breaching as a mechanism for generating sustained turbidity currents. In *33rd internation association of hydraulic engineering & research congress: Water engineering for a sustainable environment, vancouver, iahr*.

Garcia, M., & Parker, G. (1993). Experiments on the entrainment of sediment into suspension by a dense bottom current. *Journal of Geophysical Research*, *98*(C3), 4793–4807.

Koppejan, A. W., Van Wamelen, B. M., & Weinberg, L. J. H. (1948). Coastal flow slides in the Dutch province of Zeeland. In *Proceedings of the Second International Conference on Soil Mechanics and Foundation Engineering* (pp. 89–96). Rotterdam, The Netherlands, 21–23 June 1948.

Kramer, S. L. (1988). Triggering of liquefaction flow slides in coastal soil deposits. *Engineering Geology*, *26*(1), 17–31.

Lemmin, U., & Rolland, T. (1997). Acoustic velocity profiler for laboratory and field studies. *Journal of Hydraulic Engineering*, *123*(12), 1089–1098.

Mastbergen, D. R., & Schrijvershof, R. (2016). Sedimentatiepatronen plaat van walsoorden na plaatval 22 juli 2014 [in dutch].

Mastbergen, D. R., & Van Den Berg, J. H. (2003). Breaching in fine sands and the generation of sustained turbidity currents in submarine canyons. *Sedimentology*, *50*(4), 625–637.

Parker, G., Fukushima, Y., & Pantin, H. M. (1986). Self-accelerating turbidity currents. *Journal of Fluid Mechanics*, *171*, 145–181.

Parker, G., Garcia, M., Fukushima, Y., & Yu, W. (1987). Experiments on turbidity currents over an erodible bed. *Journal of Hydraulic Research*, *25*(1), 123–147.

Pedocchi, F., & García, M. H. (2012). Acoustic measurement of suspended sediment concentration profiles in an oscillatory boundary layer. *Continental Shelf Research*, *46*, 87–95.

Sequeiros, O. E. (2012). Estimating turbidity current conditions from channel morphology: A froude number approach. *Journal of Geophysical Research*, *117*, C04003. https://doi.org/10.1029/2011JC007201

Sequeiros, O. E., Mosquera, R., & Pedocchi, F. (2018). Internal structure of a self-accelerating turbidity current. *Journal of Geophysical Research: Oceans*, *123*, 6260–6276. https://doi.org/10.1029/2018JC014061

Sequeiros, O. E., Naruse, H., Endo, N., Garcia, M. H., & Parker, G. (2009). Experimental study on self-accelerating turbidity currents. *Journal of Geophysical Research*, *114*, C05025. https://doi.org/10.1029/2008JC005149

Silvis, F., & Groot, M. B. de (1995). Flow slides in The Netherlands: Experience and engineering practice. *Canadian Geotechnical Journal*, *32*(6), 1086–1092.

Van Rhee, C. (2015). Slope failure by unstable breaching. In *Proceedings of the institution of civil engineers-maritime engineering*, *168*, Thomas Telford Ltd, pp. 84–92.

Van Rhee, C., & Bezuijen, A. (1998). The breaching of sand investigated in large-scale model tests. In *Coastal engineering 1998* (pp. 2509–2519). Copenhagen, Denmark. 22–26 June 1998.

You, Y., Flemings, P., & Mohrig, D. (2012). Dynamics of dilative slope failure. *Geology*, *40*(7), 663–666.